PAPER • OPEN ACCESS

Grain boundaries are not the source of Urbach tails in Cu(In,Ga)Se$_2$ absorbers

View the article online for updates and enhancements.

Journal of Physics: Energy

Grain boundaries are not the source of Urbach tails in Cu(In,Ga)Se$_2$ absorbers

Sevan Gharabeiki[1,*] ⓘ, Muhammad Uzair Farooq[1] ⓘ, Taowen Wang[1] ⓘ, Mohit Sood[1,2] ⓘ,
Michele Melchiorre[1] ⓘ, Christian A Kaufmann[3] ⓘ, Alex Redinger[1] ⓘ and Susanne Siebentritt[1] ⓘ

[1] Department of Physics and Material Science, University of Luxembourg, Belvaux, Luxembourg
[2] AVANCIS GmbH, Otto-Hahn-Ring 6, 81739 München, Germany
[3] Helmholtz-Zentrum Berlin für Materialien und Energie (HZB), Competence Centre Photovoltaics (PVcomB), Schwarzschildstraße 3, 12489 Berlin, Germany
[*] Author to whom any correspondence should be addressed.

E-mail: sevan.gharabeiki@uni.lu

Abstract

The presence of Urbach tails in Cu(In,Ga)Se$_2$ (CIGSe) absorbers has been identified as a limiting factor for the performance of the CIGSe solar cells. The tail states contribute to both radiative and non-radiative recombination processes, ultimately leading to a reduction in the open-circuit voltage and, consequently, decreasing the overall efficiency of CIGSe devices. Urbach tails result from structural and thermal disorders. The Urbach tails can be characterized by the Urbach energy, which is associated with the magnitude of the tail states. Within polycrystalline CIGSe absorbers, grain boundaries can be considered as structural disorder and, therefore, can potentially contribute to the Urbach tails. In fact, it has been proposed that the band bending at grain boundaries contribute significantly to the tail states. This study focuses on examining the correlation between Urbach tails and the band bending at the grain boundaries. The Urbach energies of the CIGSe samples are extracted from photoluminescence (PL) measurements, which reveal that the introduction of Sodium (Na) into the material can lead to a reduction in the Urbach energy, and an even further decrease can be achieved through the RbF post-deposition treatment. The band bending at the grain boundaries is investigated by Kelvin probe force microscopy measurements. A thorough statistical analysis of more than 340 grain boundaries does not show any correlation between Urbach tails and grain boundaries. We measure small band bending values at the grain boundaries, in the range of the thermal energy (26 meV at room temperature). Furthermore, our intensity dependent PL measurements indicate that Urbach tails are, at least in part, a result of electrostatic potential fluctuations. This supports the model that the introduction of alkali elements mainly decreases the magnitude of electrostatic potential fluctuations, resulting in a subsequent reduction in the Urbach energy.

1. Introduction

Thin-film Cu(In,Ga)Se$_2$ (CIGSe) solar cells have achieved remarkable efficiencies surpassing 23.5% [1]. A key factor contributing to the improvement of efficiencies in CIGSe solar cells is the introduction of heavy alkali elements into the absorbers through alkali-fluoride post-deposition treatment (PDT) [1–5]. It has been widely known that sodium (Na) has a beneficial role in the CIGSe solar cells: primarily by enhancing net p-type doping and consequently increasing the open-circuit voltage (V_{OC}) [6–8]. Over the past decade, researchers have also explored the incorporation of heavy alkali elements such as potassium (K), rubidium (Rb) and cesium (Cs) into the CIGSe absorbers [2, 3, 5]. This approach has yielded higher efficiencies due to surface passivation, reduction of bulk recombination, increase in the p-type doping level, and decrease in the

Urbach energy [5, 7, 9–12]. The primary effect of heavy alkali-fluoride PDT is the improvement of the V_{OC}, thereby leading to an overall increase in the efficiency of CIGSe solar cells [5].

Urbach tails refer to a density of states that decays exponentially into the band gap [13], with the decay constant being equal to the Urbach energy [12, 14]. In contrast to the ideal semiconductor, where the density of states in both valance band and conduction band does not extend into the forbidden gap. Higher Urbach energies indicate an increase in density of states that extends into the forbidden gap. Part of the Urbach tails is caused by thermal motion (i.e. phonon vibrations) [13, 15, 16]. However, disorders such as bandgap fluctuations or grain boundaries (GBs) can make additional contributions [12, 15, 17–19]. Bandgap fluctuations originate from two primary sources: alloy disorder, such as the random distribution of In and Ga within the material, which leads to variation in the local band gap energy and overall fluctuations in the band gap [20], and electrostatic potential fluctuations resulting from Coulombic interactions between charged defects that can cause fluctuations in the band edges [17, 21].

The tail states contribute to both radiative and non-radiative recombination. By contributing to the non-radiative recombination (i.e Shockley-Read-Hall recombination), they can decrease the external radiative efficiency (or photoluminescence quantum yield PLQY) of the solar cell and in turn decrease the V_{OC} and efficiency of the device [12]. Additionally, the presence of Urbach tails enhances sub-bandgap absorption, resulting in a shift in the photoluminescence (PL) emission peak to lower energies than the bandgap energy [22]. These sub-band gap absorptions reduce the radiative voltage limit of the solar cells, in turn, decreasing the quasi-Fermi level splitting (ΔE_F) and V_{OC} of the device [12, 20, 22, 23].

It has recently been shown that the incorporation of alkali elements can decrease the Urbach energy of the CIGSe absorbers [5, 12, 24]. The Urbach energy decreases with the incorporation of Na, and it can be further decreased by the incorporation of heavy alkali elements such as Rb and K [4, 12, 17, 24]. The decrease in the Urbach energy was attributed to a grain boundary passivation effect [5, 12]. This phenomenon was supported by Kelvin probe force microscopy (KPFM) measurements, which reveal a significant decrease in the contact potential difference (CPD) at the GBs with the incorporation of heavy alkali elements [5, 25, 26].

The band bending observed at GBs is generally understood to be a consequence of charged defects present in these regions [27]. The proposed mechanism for the reduction in the Urbach tails involves a decrease in the amount of band bending at the GBs resulting from the accumulation of the alkali elements [5]. This accumulation may effectively eliminate charged defects, dangling bonds, copper vacancies, and other imperfections [5]. Moreover, the latest reports indicate that the passivation of GBs can also result from the annihilation of the V_{Cu}–V_{Se} divacancy complex at the GBs [28]. This reversible mechanism has been linked to the role of Na in relation to oxygen [28].

However, all these KPFM studies on the GBs were performed by amplitude-modulation Kelvin Force Microscopy (AM-KPFM) [5, 25, 26, 28–33]. Recent findings suggested that AM-KPFM measurements on the polycrystalline rough absorbers may not be as dependable as previously thought: The topographic crosstalk can potentially lead to misinterpretations of the collected data [34]. Additionally, there are no studies in the literature that directly compare the band bending of the samples without alkali elements with those containing Na and Na + Rb.

Furthermore, most recent studies indicate that the incorporation of Na and K into CIGSe single crystals, in the absence of GBs, leads to a reduction in the Urbach energy, as well [17]. The Primary effect of alkali elements in the single crystal CIGSe absorbers is a decrease of the degree of compensation and therefore decrease in the magnitude of electrostatic potential fluctuations which leads to decrease in the Urbach energy [17]. Therefore, we critically review the effect of different alkalis on GBs and tail states.

We study Cu(In,Ga)Se$_2$ absorbers and solar cells without the addition of alkali elements, with only Na added and with Na + Rb added. We extract the Urbach energy and the ΔE_F from the PL measurements. The impact of alkali incorporation on the work function and grain boundary band bending is investigated through frequency-modulation KPFM (FM-KPFM) measurements. The KPFM measurements show a weak band bending along the GBs, and surprisingly, these measurements did not reveal a correlation between the band bending at the GBs and decrease in the Urbach energy. Furthermore, intensity dependent PL measurements suggest that the primary effect of alkali incorporation is a reduction in the magnitude of electrostatic potential fluctuations within the grains, consequently leading to a decrease in the Urbach energy. A model previously proposed for single-crystalline CIGSe absorbers can be employed to explain the decrease in the magnitude of electrostatic potential fluctuations, which is attributed to the increase in the net doping concentration and decrease in the degree of compensation [17].

Table 1. Sample properties: sample name, alkali presence, CGI and GGI values, band gap energy (E_g), and photovoltaic parameters of the solar cell with highest efficiency in each series.

Deposition series	Sample name	Alkali	PDT	CGI	GGI	E_g^b (eV)	V_{OC} (mV)	J_{SC} (mA cm^{-2})	FF	Eff (%)
A	A1	None	No	0.95	0.28	1.15	526	34	66.4	11.8
	A2	Na	No	0.97	0.21	1.10	627	36	74	16.7
	A3	Na + Rb	RbF *in-situ*	0.98	0.20	1.09	673	36.1	77.4	18.8
B	B1	Na	No	0.97	0.23	1.11	587	34.6	71.7	14.5
	B2^a	Na + Rb	RbF *ex-situ*	0.96	0.22	1.11	—	—	—	—

^{a} *Ex-Situ* PDT results in shunted devices.

^{b} The band gap (E_g) was extracted from Gaussian fit to first derivative of absorptance (see figure S2 in supporting information). Different fitting ranges were employed, and the errors of determined band gap is $\pm$ 3 meV.

2. Results and discussion

2.1. Impact of alkalis on the device performance and Urbach energy

Overall, five samples were investigated. The samples were processed using a multistage co-evaporation method described in detail elsewhere [11, 35]. For the samples containing Na, the deposition was performed on Mo coated soda lime glass (SLG) and Na naturally diffused into the absorbers from substrate. The Na free samples were prepared with Na barrier (SiO_xN_y) to stop the Na diffusion from SLG into the absorber.

Table 1 displays the key properties of the samples in this study. For samples in the 'A series' subjected to RbF PDT, an *in-situ* PDT was applied. Meanwhile, the samples in the 'B series' received *Ex-situ* RbF PDT. More details regarding the sample preparation and PDT process are explained in the experimental section. All samples show Cu-poor composition ($\frac{Cu}{Ga+In}$ (CGI) <1). The sample deposited on substrate with Na-Barrier (i.e. no alkalis) show higher $\frac{Ga}{Ga+In}$ (GGI) values, resulting in higher band gap energy (E_g). The E_g of each sample was determined from inflection point of the absorptance $A(E)$ spectra [22]. (See experimental section and figure S2(d) in supporting information)

Moreover, solar cells were fabricated using the absorbers from each series. Figure 1 depicts device performance of the solar cells made from series *A* absorbers. The J-V characteristics of the solar cell with highest efficiency on each absorber are shown in figure 1(a), and the corresponding device parameters are summarized in table 1. Furthermore, the statistical distributions of photovoltaic parameters are illustrated in figures 1(b)–(e).
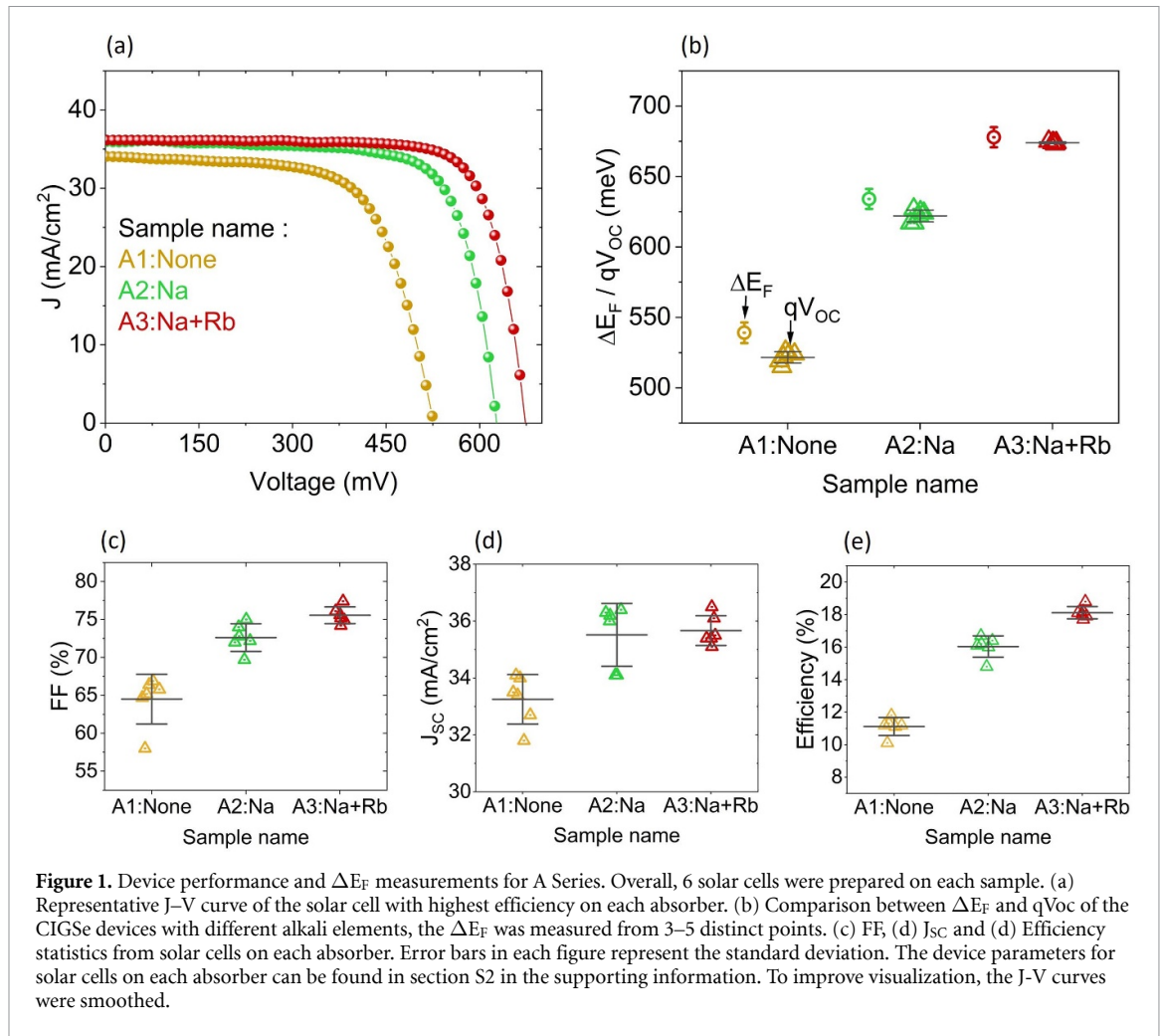
In figure 1(b) we compare the ΔE_F with the average qV_{OC} of the solar cells. It is important to highlight that the ΔE_F values were extracted from linear fit to the high energy slope of the Planck's generalized law where the absorptance is assumed to be one [22, 36], and all measurements were conducted under 1 sun equivalent illumination condition using 660 nm laser. In this case the ΔE_F is the upper limit of the qV_{OC}, allowing for a direct comparison between ΔE_F and qV_{OC} [36]. We observe that samples without alkali elements show the lowest ΔE_F and the lowest V_{OC}. With the incorporation of Na, the ΔE_F and V_{OC} improve, and samples with additional RbF PDT show the highest ΔE_F and V_{OC} values. The ΔE_F improvement can also be observed for samples in B-Series. (See figure S3(a) in supporting information)

Figure 2(a) depicts the absorption coefficient of the A-series samples, extracted from PL measurements within the energy range lower than the band gap energy (E_g). The Urbach energy (E_U) is extracted from the exponential decay of the absorption coefficient as $\alpha \sim \exp(E/E_U)$. As previously reported [12, 24], the introduction of Na results in a significant decrease in the Urbach energy. Furthermore, RbF PDT leads to a small decrease in the Urbach energies for A series samples ($\sim$0.5 meV decrease). On the other hand, *ex-situ* RbF PDT treatment on the B series results in a stronger reduction in the Urbach energy (figure 2(b)).

Recent studies established an empirical linear correlation between Urbach energy and voltage loss (qV_{OC}^{Loss}) for Perovskite and CIGSe solar cells [12, 37]. qV_{OC}^{Loss} or ΔE_F^{Loss} refers to the difference between measured $qVoc$ or ΔE_F and Shockley–Quisser qV_{OC} limit (qV_{OC}^{SQ}) [12, 38]. (See figure 2(c) inset). In figure 2(c), gray color points show the linear correlation between Urbach energy and qV_{OC}^{Loss} for state-of-the-art (SOA) CIGSe absorbers [12].

In the perfect scenario, ΔE_F and the qV_{OC} would be identical. However, the presence of interface recombination can lead to a gradient in the quasi-Fermi level of minority carriers near the interface, and this gradient can push the qV_{OC} below the ΔE_F [36, 39]. Notably, it was previously shown that for SOA CIGSe samples, with optimized interface properties, ΔE_F and qV_{OC} have almost identical values [38, 40].

In figure 2(c), we compare the ΔE_F^{Loss} of our samples with the qV_{OC}^{Loss} of the SOA CIGSe solar cells. The qV_{OC}^{SQ} of each sample was calculated from band gaps reported in table 1. (See also table S1 in the supporting information). In our study, the samples exhibit higher values of the ΔE_F^{Loss} in comparison with the SOA

Figure 1. Device performance and ΔE_F measurements for A Series. Overall, 6 solar cells were prepared on each sample. (a) Representative J–V curve of the solar cell with highest efficiency on each absorber. (b) Comparison between ΔE_F and qVoc of the CIGSe devices with different alkali elements, the ΔE_F was measured from 3–5 distinct points. (c) FF, (d) J_{SC} and (d) Efficiency statistics from solar cells on each absorber. Error bars in each figure represent the standard deviation. The device parameters for solar cells on each absorber can be found in section S2 in the supporting information. To improve visualization, the J-V curves were smoothed.

samples at comparable Urbach energy values. The fact that the data points are further from the empirical line, suggests that in our samples, the Urbach tails are not the limiting factor contributing to the ΔE_F^{Loss}. The higher ΔE_F^{Loss} might be attributed to the presence of additional non-radiative recombination centers other than Urbach tails, or lower doping concentration compared to SOA CIGSe samples. The alkali incorporation has dual impact on the CIGSe absorbers. Part of the increase in ΔE_F is due to the passivation of non-radiative recombination centers through incorporation of alkali elements (i.e. increase in the minority carrier lifetime). The lifetime measurements on our samples show significant increase with the incorporation of alkali elements (see figure S5 in the supporting information). However, the alkali incorporation can also enhance the ΔE_F by increasing the doping concentration of material. Notably, in CIGSe samples with a similar band gap to our absorbers (1.1 eV) but higher V_{OC} and efficiency, capacitance–voltage (C–V) measurements show doping values around 2–5×10^{16} cm^{-3} [41, 42]. On the other hand, in our samples the doping concentration extracted from C–V measurements is approximately one order of magnitude lower than the reported values for high efficiency CIGSe solar cells. (See figure S6 in the supporting information)

2.2. KPFM measurements and grain boundaries

To further investigate the effect of GBs on the tail states, FM-KPFM measurements were conducted on the samples. To prevent surface oxidation, all measurements were performed in the nitrogen atmosphere with relative humidity less than 10%. It has been recently reported that ammonia cleaning is essential for the KPFM measurements in order to remove precipitates originating from the PDT treatment [9] (see figure S7 in the supporting information). Consequently, for all the measurements presented in the following, the samples underwent a 30 s cleaning process using 1 molar ammonia solution to remove possible surface oxides and Rb-containing compounds.

Figure 3 depicts representative AFM measurements carried out on the A series, where the topography is shown in the first row and corresponding work function map in the second row. The surface morphology (figures 3(a)–(c)) shows grains with the size of 1–2 μm. The alkali-free sample and the absorber with Na
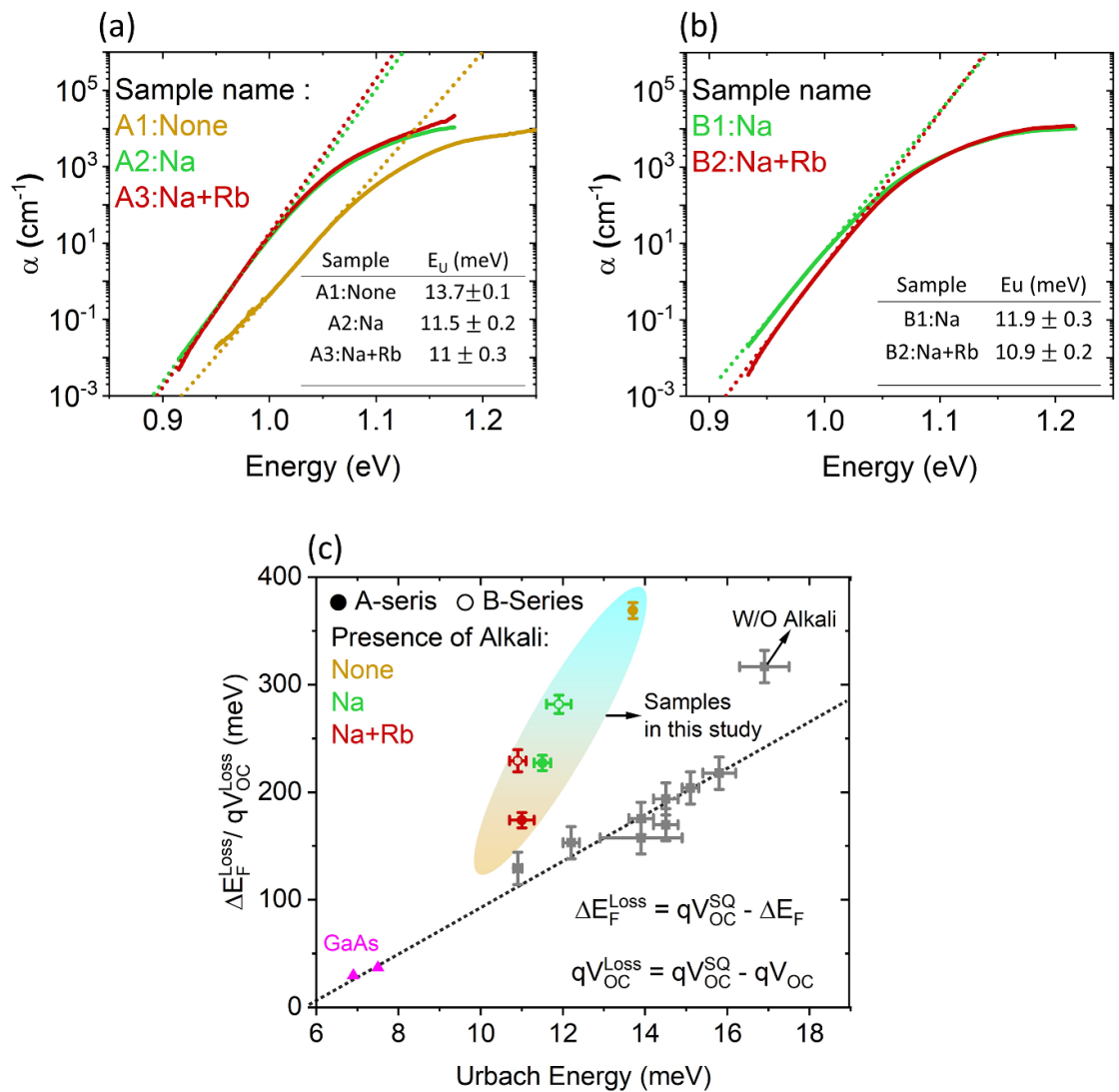
Figure 2. (a) and (b) Absorption coefficient extracted from PL of the samples from series A and B respectively. The Urbach energy (E_U) were extracted from exponential decay of the absorption coefficient within the band gap energy. Three different fitting ranges were applied, and the average value is reported in the table. Laser light with same incident intensity was used for Urbach energy extraction. (c) Comparison of the ΔE_F^{Loss} of the samples in this study with qV_{OC}^{Loss} of the states-of-the-art (SOA) CIGSe solar cells (shown in gray color from), all SOA CIGSe samples follow the empirical line, except the sample without any alkali elements. The filled circles represent samples from A series, while the open circles illustrate samples from B series. Purple triangles are GaAs samples which are reference samples in this graph with the lowest Urbach energy. Average values of Urbach energy and ΔE_F^{Loss} or qV_{OC}^{Loss} are presented here. And the errors bars represent the standard deviation (This graph is modified version of figure 4 reproduced from [12]. CC BY 4.0).

show average work function of 4.83 ± 0.05 eV and 4.66 ± 0.16 eV, respectively. The values are in reasonable agreement with previous studies carried out on polycrystalline and single crystalline CIGSe absorbers with or without presence of Na [9, 34]. Moreover, in all samples certain areas show slightly higher work functions (White dots). In the A1 sample deposited on substrate with Na-barrier (i.e. without alkali) these regions with higher work function are more prevalent. The origin of these precipitations is not clear at present. Furthermore, the RbF treated samples show a higher average surface work function with the average value of 5.47 ± 0.22 eV. The increase in the surface work function can be attributed to the surface modification after RbF PDT.

The surface modification following heavy alkali PDT was reported in previous studies [2, 5, 9, 43, 44]. Some early reports suggested that thin Rb–In–Se layer is formed after RbF PDT [5, 43, 44]. However, recent studies proposed that the surface modification is due to the exchange mechanism between Rb and Cu and the subsequent formation of Rb-rich ordered defect compound phases at the surface [9].

On the other hand, the influence of *ex-situ* RbF PDT on the B series is different (See figure S8 in the supporting information). The surface work function for these samples does not exhibit a similar increase after RbF PDT. It is plausible that factors such as air exposure prior to the PDT or higher substrate temperature that is used during the *ex-situ* PDT may impact surface modification, leading to different results.
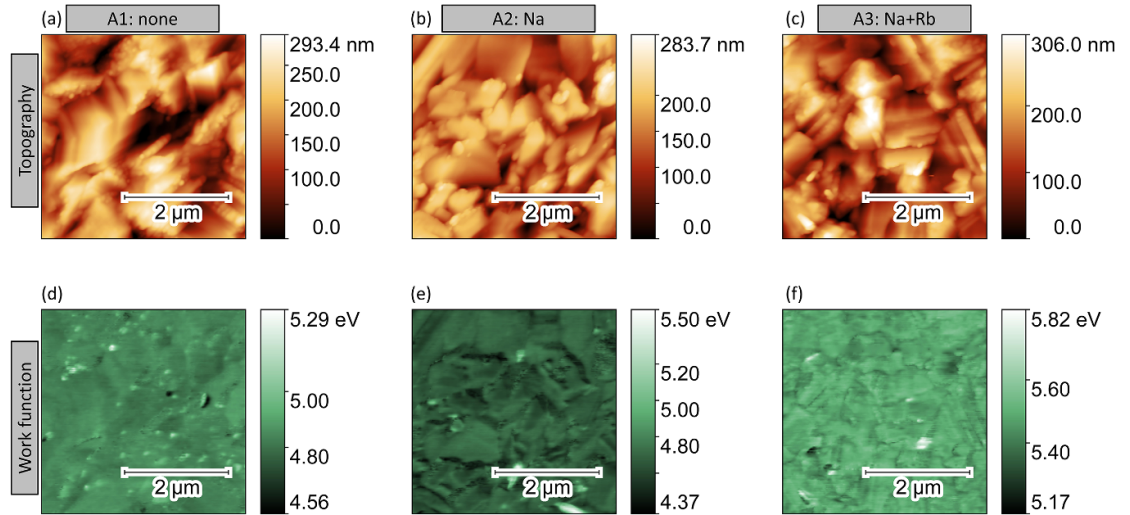
Figure 3. Topography images measured by AFM and simultaneous KPFM measured work function for CIGSe samples from A series. (a), (d) samples with no alkali. (b), (c) samples containing Na and (c), (f) samples with Na + Rb.
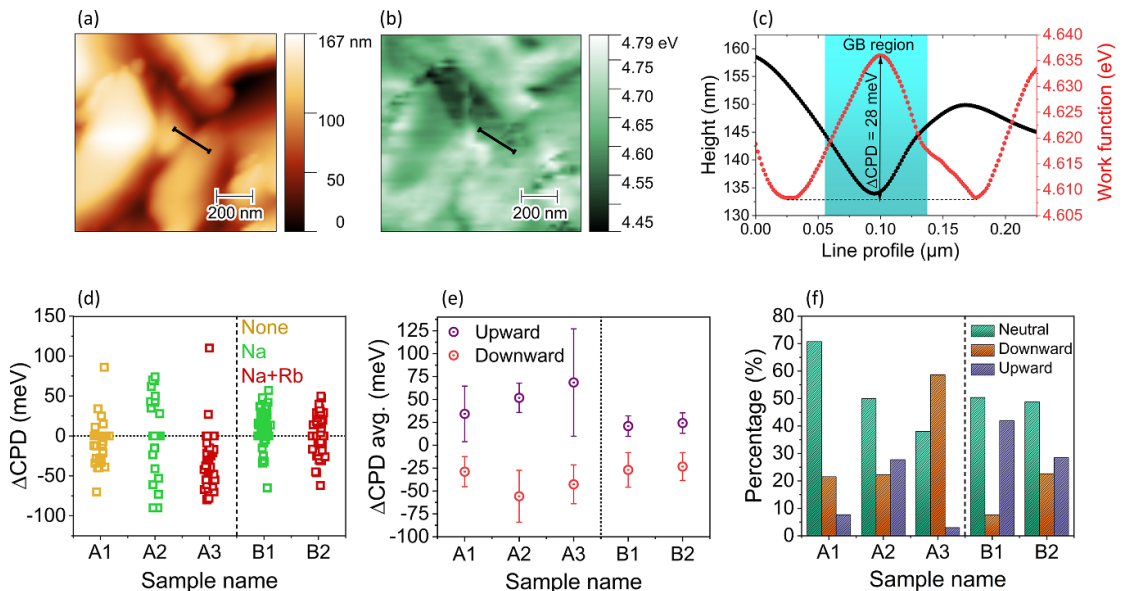

Figure 4. (a) and (b) Selected GB from the A2 sample shown with line across the GB. (a) shows the topography image and (b) shows the simultaneous acquired work function map. (c) line profile across the grain boundary as indicated in (a) and (b), showing measured ΔCPD with 28 meV upward band bending. (d) The contact potential difference across the GBs of the CIGSe samples. Positive values denote upward band bending, while negative values indicate a downward band bending. Neutral GBs exhibit no change in band bending across them. (e) Average amount of band bending across the GBs for samples with different alkali incorporation. A3 sample just shows 2 out of 67 GBs with Upward band bending. However, the average amount is shown with substantial error bars. (f) Bar chart indicating statistics of the GBs with different alkali elements.

Furthermore, the band bending across the GBs can be extracted from the change in the CPD (or work function) between grains and GBs. To characterize the band bending at the GBs, first we identify the grain boundary position from topography profile (figure 4(a)), and then copied to the KPFM map to extract the changes in work function (figure 4(b)). Subsequently the band bending at the GBs (ΔCPD) can be extracted from the line profile. (Figure 4(c)).

In figure 4(d), the extracted ΔCPD from GBs in each sample is illustrated. The positive values indicate upward band bending while the negative values indicate downward band bending, and neutral GBs with ΔCPD = 0 show no measurable band bending across them. Here a threshold of less than 10 meV was used. Overall, we analyzed 340 GBs to ensure that our statements are statistically reliable. In the experimental section and supporting information more details can be found regarding the band bending analysis. (See figure S9 in the supporting information)

Figure 4(e) shows the average value of band bending, separately for the GBs with downward and upward band bending. It can be seen that the average value is very small, within the range of thermal energy (26 meV at room temperature), and it hardly changes for different samples. Within error, the average amount of band bending is unchanged with or without different alkali incorporation.

Figure 4(F) illustrates the share of upward, downward, and neutral GBs for each sample. In samples without any alkali element, the dominant number of GBs are neutral. However, upon introducing Na, there is an increase in the number of GBs with upward band bending. The distribution is still dominated by neutral GBs. This observation is in line with the previous reports that the segregation of Na at the GBs increases the number of GBs with upward band bending [45, 46]. Moreover, samples with RbF PDT, result in a substantial increase in the GBs with downward band bending, accompanied by a significant decrease in the number of GBs exhibiting upward band bending.

On the other hand, we did see significant changes in the Urbach energies with the introduction of alkali elements. Thus, the KPFM measurements do not reveal a correlation between Urbach tails and the GBs. First of all, the amount of band bending remains small, even for the alkali free sample (figure 4(e)). Secondly, with the introduction of alkalis, the share of neutral GBs decreases (figure 4(f)), this observation indicates that the introduction of alkalis results in higher number of charged defects at the GBs and, consequently, more charged GBs. If there was a correlation between Urbach tails and GBs, one would expect lower band bending and less number of charged GBs for the alkali containing samples. We can conclude, that it is not changes at the GBs that explain the reduction in tail states in Cu(In,Ga)Se$_2$ upon alkali addition. This agrees with the observation that tail states are reduced by alkali treatments even in single crystalline films [17]. However, we would like to note that the current KPFM analysis results are limited to the near surface region as the KPFM measurements are surface sensitive.

In the following we discuss the reason for the reduction of tail states by alkali addition, independent of GBs.

2.3. Electrostatic potential fluctuations and intensity dependent PL measurements

The Urbach tails are due to disorder. The disorder is due, in part, to lattice vibrations (i.e. thermal effects); structural defects make additional contributions. The model was proposed by Cody *et al* [15] to describe the temperature dependent behavior of the Urbach Energy (E_U) in the presence of structural disorders:

$$E_U = S_0 k \theta_E \left(\frac{1+X}{2} + \frac{1}{\exp\left(\frac{\theta_E}{T}\right) + 1} \right). \tag{1}$$

Where S_0 is a constant, k denotes the Boltzmann constant, T the temperature, θ_E is Einstein characteristic temperature, and X is a dimensionless parameter independent of temperature which denotes the magnitude of structural disorders, in a perfect crystal without the presence of structural disorders, X is expected to be zero [15, 16, 47].

The temperature dependent Urbach energies has been measured to extract the degree of structural disorders (X) in materials such as perovskites [48], GaAs [16] and InP [47]. However, the case of CIGSe semiconductors is more complicated. Some reports have attempted to determine the structural disorder parameter (X) for CuInSe$_2$ (CISe) single crystals [49, 50]. However, it has been observed that the temperature dependent Urbach energy for CISe does not follow the equation (1) [49].

In Cu-poor CIGSe absorbers, electrostatic potential fluctuations have an influence on the density of states within the band gap [21, 51], consequently affecting the magnitude of Urbach energy [52]. Cu poor CIGSe is a compensated semiconductor [17, 21, 51–55]. Within these materials, both charged donors and acceptors are distributed randomly, exerting Coulombic forces that lead to the distortion of band edges by electrostatic potential fluctuations [55]. In this case, the density of states within the band gap of the CIGSe absorbers is not solely linked to structural disorder, but is due to temperature dependent potential fluctuations. This means in equation (1), X becomes temperature dependent. Since we do not consider $E_U(T)$ in detail, we did not try to include this temperature dependence in equation (1).

The magnitude of electrostatic potential fluctuations can be influenced by the laser excitation intensity and by temperature [17, 21, 56]. With the increase in the laser excitation, the photogenerated charge carriers neutralize charged defect and screen the charges, consequently reducing the amplitude of electrostatic potential fluctuations (figure 5(a)) [21, 51]. Similarly, as the temperature rises, thermally generated charge carriers can also screen the charged impurities, resulting in a reduction in the magnitude of electrostatic potential fluctuations [56]. The magnitude of electrostatic potential fluctuations has been investigated by temperature dependent PL measurements [17, 56]. It was reported that in the CIGSe absorbers the electrostatic potential fluctuations are flattened with increasing temperature [17, 56]. Still, in Cu-poor
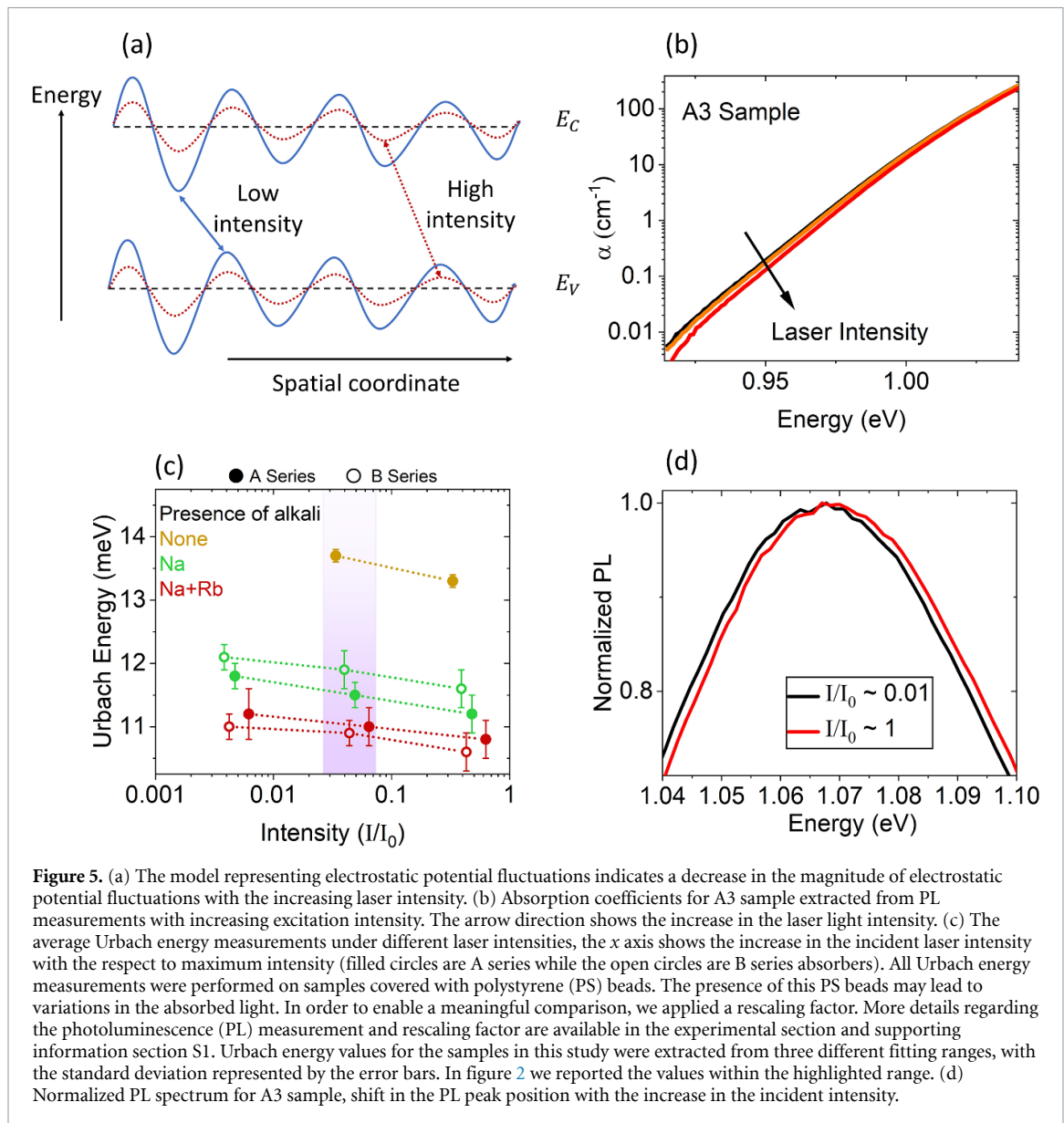
Figure 5. (a) The model representing electrostatic potential fluctuations indicates a decrease in the magnitude of electrostatic potential fluctuations with the increasing laser intensity. (b) Absorption coefficients for A3 sample extracted from PL measurements with increasing excitation intensity. The arrow direction shows the increase in the laser light intensity. (c) The average Urbach energy measurements under different laser intensities, the *x* axis shows the increase in the incident laser intensity with the respect to maximum intensity (filled circles are A series while the open circles are B series absorbers). All Urbach energy measurements were performed on samples covered with polystyrene (PS) beads. The presence of this PS beads may lead to variations in the absorbed light. In order to enable a meaningful comparison, we applied a rescaling factor. More details regarding the photoluminescence (PL) measurement and rescaling factor are available in the experimental section and supporting information section S1. Urbach energy values for the samples in this study were extracted from three different fitting ranges, with the standard deviation represented by the error bars. In figure 2 we reported the values within the highlighted range. (d) Normalized PL spectrum for A3 sample, shift in the PL peak position with the increase in the incident intensity.

chalcopyrite, as ours, a reduced amount of electrostatic fluctuations remains even at room temperature [56]. In our study, we have conducted intensity-dependent PL measurements at room temperature (296 K) to observe the impact of electrostatic potential fluctuations on the Urbach energy of the CIGSe samples.

Figure 5(b) displays the absorption coefficient of the *A3* sample obtained from intensity dependent PL measurements. The measurements were conducted at room temperature ($\sim$ 296 K) and the incident laser intensity was increased by factor of 10 in each step. It is evident that even at room temperature, electrostatic fluctuations are present in the CIGSe absorbers: As the intensity increases, the Urbach energy decreases. A similar behavior has been observed for the other samples. In figure 5(c) we summarize the intensity dependent Urbach energy values for all samples. The decrease in the Urbach energy with the increase in the incident light intensity indicates that the density of states within the band gap is at least partially caused by electrostatic potential fluctuations. Moreover, the PL spectrum shows a small blue shift with increasing intensity (figure 5(d)), this shift is attributed to the flattening of the electrostatic potential fluctuations, leading to a decrease in Urbach energy and, consequently, increase in the PL transition energy [17, 38, 56]. If the Urbach tails solely arose from static disorders such as the alloy disorder, the increase in the laser intensity would not change the band gap fluctuations and would not lead to a decrease in the Urbach energy. Thus, the observation that the Urbach energy decreases with increasing excitation flux suggests that Urbach energies are at least partly due to electrostatic fluctuations.

The average depth of the electrostatic potential fluctuations can be described according to the following equation [57].
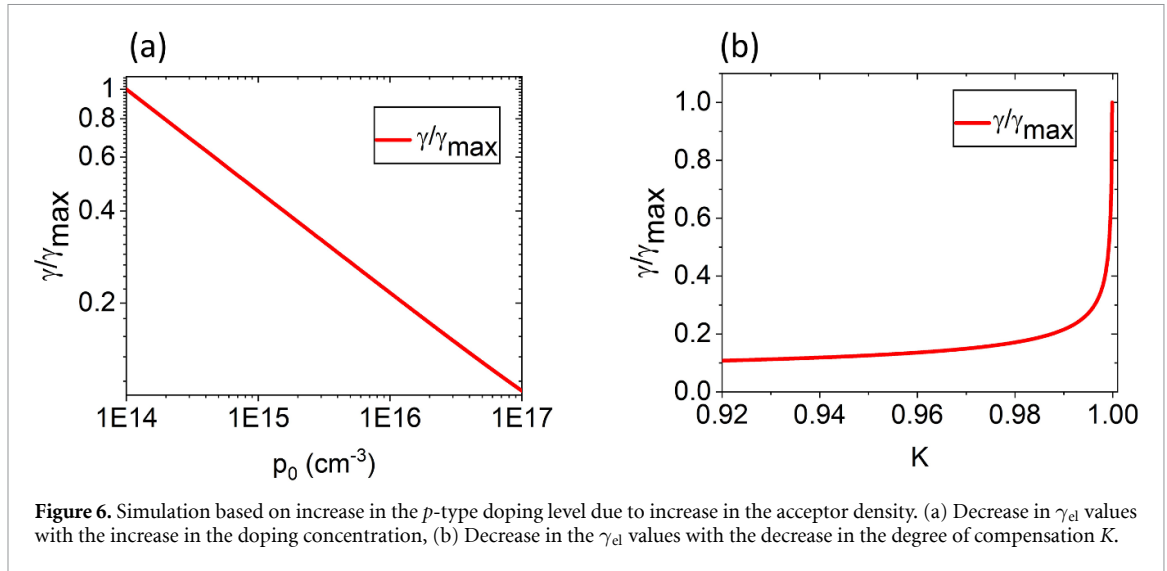
Figure 6. Simulation based on increase in the *p*-type doping level due to increase in the acceptor density. (a) Decrease in γ_{el} values with the increase in the doping concentration, (b) Decrease in the γ_{el} values with the decrease in the degree of compensation *K*.

$$\gamma_{el} = \frac{e^2}{4\pi\varepsilon_0\varepsilon}\frac{N_I^{2/3}}{p^{1/3}}. \tag{2}$$

Where N_I is the sum of charged donor and acceptor density, e denotes elementary charge, ε_0 vacuum permittivity, ε is the relative permittivity of the semiconductor, p is the density of mobile carriers (holes and electrons) and can be defined as $p = p_0 + \Delta p + \Delta n$ where p_0 is the net doping concentration ($N_A - N_D$), while $\Delta n = \Delta p$ are the photogenerated carrier densities [58]. The larger γ_{el} values would result in more density of states that extend within the band gap, and thus, higher Urbach energies [21, 59]

For each individual sample with increasing laser intensity, the number of photogenerated carriers increases, resulting in a decrease in the magnitude of electrostatic potential fluctuations and thus in a reduction of Urbach energy—as observed in figures 5(b) and (c).

The first scenario for decrease in the depth of electrostatic potential fluctuations is decrease in the number of charged defects (N_I) with the incorporation of alkali elements. According to equation (2), at the constant doping concentration with the decrease in the N_I, one would have expected the reduction for γ_{el} values.

The second proposed mechanism is based on decrease in the degree of compensation and subsequent increase in the doping concentration which can lead to decrease in the γ_{el} values [17]. According to equation (2) samples with higher doping concentration should show lower γ_{el} values. (See below and section S8 in the supporting information).

Alkali treatments increase the net doping in chalcopyrite [6, 8, 11, 60, 61]. For the effect of Na several mechanisms have been proposed: One mechanism suggests that Na increases the density of copper (Cu) vacancies, which act as acceptors, thereby enhancing doping due to the higher number of acceptors [61]. Another mechanism proposes that Na decreases the In_{Cu} antisite donors [6, 60, 62]. Recent studies suggest that Na facilitates the migration of In_{Cu} antisites from the grain interior to GBs, thereby reduces the compensation within the grains and increases the doping level [62].

We define the degree of compensation as

$$K = \frac{N_D}{N_A} \tag{3}$$

where N_D and N_A are the donor and acceptor concentration respectively.

Although the exact mechanism behind the increase in the doping concentration is not clear, both mechanisms: increase in the acceptor concentration (N_A) and decrease in the donor concentration (N_D) can effectively decrease the degree of compensation.

Studies on CuGaSe$_2$ absorbers have reported the *K* values close to 0.99 [63]. By assuming that the $N_I = N_A + N_D$ and $p_0 = N_A - N_D$, the reduction in the magnitude of electrostatic potential fluctuations, correlated with an increase in the doping density and a decrease in the compensation, can be modeled using equation (2). In figure 6 we simulated the effect of increase in doping with increase in the acceptor density (N_A) on the γ_{el} values. Here we assume that N_D is constant, and we increase the N_A which leads to subsequent increase in the doping concentration and reduction of γ_{el} values. Similar simulations can be performed based on constant N_A and decrease in the N_D values. More details regarding the simulations can be found in the supporting information (see section S8 in supporting information).

The increase in net doping was already proposed to explain the reduction in electrostatic potential fluctuations and Urbach tails in single-crystalline CIGSe films [17]. The measured C–V doping profiles for A series samples are illustrated in figure S6 in the supporting information. The doping level shows a significant increase with the incorporation of Na and a small increase can be seen with the incorporation of Rb. A similar increase in the doping level with the RbF PDT was previously reported for similarly processed absorbers with C–V measurements [11]. Unfortunately, change in the doping level was not possible to analyze on B series absorbers, since *ex-situ* RbF PDT results in a shunted device on *B*2 absorber.

Moreover, as the depth of electrostatic potential fluctuations decreases, it is expected that the samples show more laterally homogeneous doping distribution [42, 64]. (See section S9 in supporting information). The most recent investigations using conductive atomic force microscopy tomography technique confirm that heavy alkali PDT results in a higher and more uniform doping distribution across the CIGSe absorbers [41].

3. Conclusion

CIGSe absorbers without alkali incorporation, with Na and with Na + Rb were investigated in this study. The ΔE_F increases with the incorporation of alkali elements, the samples with RbF PDT show the highest ΔE_F. The Urbach energy decreases from samples without alkali to samples with Na and further reduction in the Urbach energy was observed for the samples with Na + Rb, as was observed before. It was proposed that this reduction of tail states is due to a reduction on band bending at GBs [5]. However, our KPFM measurements, based on the FM technique in nitrogen, indicate only weak band bending at the GBs, even for the alkali-free sample. If there is any change with alkali treatment, the number of neutral GBs decreases. Therefore, there is no correlation between Urbach tails and the band bending at GBs. Moreover, with intensity dependent PL measurements we could confirm that at least part of the density of states within the bandgap are in fact due to the presence of electrostatic potential fluctuations. The reduction in the Urbach energy with alkali addition is a result of a decrease in the average depth of electrostatic potential fluctuations due to decrease in the number of charged point defects within the grains or a higher net doping in the CIGSe absorbers.

4. Experimental section

4.1. Sample preparation
The CIGSe absorbers were prepared at PVComB using a modified 3-stage co-evaporation method, with the maximum substrate temperature of 530 °C [11, 35]. The samples were deposited on Mo coated SLG. In cases where the samples contained Na, the Na naturally diffused into the absorbers from SLG. For samples without Na, Prior to Mo deposition, a Na barrier was deposited on SLG to prevent Na diffusion. For the *in-situ* RbF treatment, following the deposition process, the substrate temperature was decreased to 280 °C. Subsequently, RbF was evaporated onto the absorbers' surface for a duration of 10 min in the presence of Se. In the case of *ex-situ* PDT, following the deposition process, the samples are taken out of the vacuum chamber and subsequently divided into two parts. One part was kept as a reference and the other part was re-introduced into the vacuum chamber and received RbF-PDT at the temperature of 480 °C for 10 min. Selenium pressure for PDT is decreased to one-sixth of the selenium pressure used during the growth phase. To minimize the surface oxidation and contamination, the samples were transferred to University of Luxembourg within a vacuum-sealed bag. The composition of the samples was determined using energy dispersive x-ray spectroscopy with an acceleration voltage of 20 kV.

4.2. Solar cell preparation
The CdS was deposited as a buffer layer by chemical bath deposition. Before CdS deposition, to remove possible surface oxides and contaminations, all samples underwent a rinsing process with 1 Molar ammonia solution. More details regarding the CdS deposition can be found elsewhere [65, 66]. After the CdS deposition, sputtered i-ZnO/Al:ZnO was sequentially deposited on the surface followed by Al–Ni grids deposition by e-beam evaporation.

4.3. Current—voltage (J-V) measurements
The J-V measurements were performed at the temperature of 25 °C, using a 4-probe configuration within a solar simulator. The simulator provides a simulated AM 1.5 spectrum and was calibrated using a Si reference cell for accurate characterization.

4.4. Photoluminescence measurements (PL)
For ΔE_F extraction, the PL measurements were conducted at the room temperature (here 296 K) under the 1 sun incident photon flux density. A diode laser with the wavelength of 660 nm and the beam radius of

1.1 mm was used to excite the samples. To prevent surface degradation, all measurements were carried out on CdS covered samples. The PL signal was collected using two off axis parabolic mirrors and was directed to spectrometer where it was detected by InGaAs detector. Subsequently, the commercially available halogen lamp spectrum was used to spectrally correct the PL spectrum. The InGaAs detector is equipped with two detector diodes. To ensure greater accuracy and to mitigate the influence of different sensitivities between the two diodes, only the points extracted from a single diode are used. Moreover, the ΔE_F values were extracted from a linear fit to the high-energy flank of Planck's generalized law where we assumed that the absorptance is equal to one [22, 67]. This assumption can induce systematic errors around 5 meV for ΔE_F. Additional details regarding the errors and ΔE_F extraction will be provided in the future publications [68]. The PL measurements were performed on several distinct points for each sample and average ΔE_F values were reported in this study. For the error bars in our study, both systematic errors and errors due to inhomogeneities of ΔE_F across the absorbers are considered.

The PL spectrums show interference fringes. The presence of interference effect was reported previously for SOA CIGSe absorbers [12, 38]. The interference effect does not influence the high energy flank of PL spectrum and ΔE_F can be reliably extracted from linear fit to Planck's generalized law as explained in previous part. However, it can distort the low energy PL decay. To remove the interference effect for Urbach energy extraction, all samples were covered with polystyrene (PS) latex beads as explained in [38]. (See figure S2 in supporting information)

The Urbach energy was extracted under different laser intensities. For intensity dependent Urbach energy extraction, an optical lens was used that decreases the beam radius to 70 μm. During the intensity dependent measurements, the absorber temperature stays at room temperature ($\sim$296 K). The Planck's generalized law was employed to extract the absorptance (A(E)) spectra, and the absorption coefficient was subsequently determined using Beer–Lambert's law [69]. The Urbach energy was then extracted from the exponential decay of the absorption coefficient at energies below the band E_g [12, 69]. Since the samples were covered by PS beads, and the PS beads cannot be coated identically on all samples, the absorbed photon flux is not same for each sample. In order to compare the Urbach energies at the similar incident laser intensities, the samples were measured before and after PS deposition. The PL spectra of the PS-covered samples were then scaled to match those without the PS layer, and the rescaling factor was determined. Subsequently, this rescaling factor was multiplied to the incident light intensity. For comprehensive details on the ΔE_F, Urbach energy measurements and intensity dependent PL measurements readers are directed to the supporting information section S1.

Additionally, absorptance $A(E)$ spectra extracted from PL measurements can be used to determine the photovoltaic band gap. (Figure S2(d) in supporting information)

4.5. Time-resolved photoluminescence measurements (TRPL)

TRPL measurements employ time-correlated single photon counting to analyze the PL decay over time. A pulsed laser operating at a wavelength of 640 nm was used to excite the samples. All measurements were conducted under identical conditions, with an injection level of approximately $\sim 10^{16}$ *photons* cm^{-3}, enabling a direct comparison of the absorbers. The TRPL measurements are illustrated in figure S5 in the supporting information.

4.6. Kelvin probe force microscopy measurements (KPFM)

Before conducting the measurements, a standardized procedure was implemented for all samples. Initially, each sample underwent a 30 s cleaning process in 1 molar ammonia solution, followed by a rinsing with water. This step is crucial to remove possible oxides, contaminations, and remaining traces of RbF. Subsequently, the samples, with the water on surface, were transferred to a nitrogen (N$_2$) atmosphere where they were allowed to dry. This process is essential to prevent both surface oxidation and contamination. To ensure the accuracy of the measurements and prevent potential contamination from the surrounding atmosphere.

AFM/KPFM measurements were done, using a Nasoscope *V* with amplitude modulation (A.M) for topography measurements. Conductive AFM tips from 'OPUS' with a platinum coating for electrical contact were used in this study, having an apex radius of less than 20 nm.

The KPFM measurements were done in a single pass closed loop, where the CPD and topography were measured simultaneously. An alternating AC voltage was applied to the sample, which generates sidebands close to the resonance of the cantilever. A lock-in amplifier was used to track these sidebands, which can be nullified when applying a specific DC voltage to the sample. This procedure allows to compensate the electrostatic force gradient between tip and sample. The DC bias is equal to the CPD which can be used to deduce the work function. To calibrate the tip work function, highly oriented pyrolytic graphite with a known work function of 4.6 eV was used.

All the CPD measurements were done in frequency modulation (FM), preferred over amplitude modulation (AM) due to its sensitivity to the force gradient, which gives better lateral resolution. In addition, the CPD measurements done in AM can be highly influenced by the topography [34].

340 GBs were identified and examined for the local potential variations. For all the samples, statistics were performed for positive and negative potential variations as well as for the neutral GBs. For more detail on the band bending extraction at the GBs, the readers are referred to [34] and figure S9 in supporting information.

4.7. Capacitance–voltage (C–V) measurements

The C–V measurements were conducted to extract the doping concentration of the CIGSe samples. The measurements were performed in dark. In order to obtain the relaxed state, the samples were kept in dark over night at 320 K, before the measurement. The C–V measurement were performed with the frequency of ~630 kHz at 100 K for samples with Na and Na + Rb, and at 160 K for sample with no alkali. The measurements were performed at low temperatures to avoid the contribution of deep defects to the capacitance. The apparent doping density vs apparent depth profile extracted from C–V measurements are illustrated in supporting information figure S6.

Data availability statement

The data that support the findings of this study are openly available at the following URL/DOI: https://doi.org/10.5281/zenodo.12799089.

ORCID iDs

Sevan Gharabeiki ● https://orcid.org/0009-0002-5696-1831
Muhammad Uzair Farooq ● https://orcid.org/0009-0003-6624-0138
Taowen Wang ● https://orcid.org/0000-0003-3081-4796
Michele Melchiorre ● https://orcid.org/0000-0003-0536-907X
Christian A Kaufmann ● https://orcid.org/0000-0001-9168-2032
Alex Redinger ● https://orcid.org/0000-0002-2958-3102
Susanne Siebentritt ● https://orcid.org/0000-0001-6522-1427

References

[1] Keller J, Kiselman K, Donzel-Gargand O, Martin N M, Babucci M, Lundberg O, Wallin E, Stolt L and Edoff M 2024 High-concentration silver alloying and steep back-contact gallium grading enabling copper indium gallium selenide solar cell with 23.6% efficiency *Nat. Energy* **9** 467–78
[2] Chirila A *et al* 2013 Potassium-induced surface modification of Cu(In,Ga)Se₂ thin films for high-efficiency solar cells *Nat. Mater.* **12** 1107–11
[3] Jackson P, Wuerz R, Hariskos D, Lotter E, Witte W and Powalla M 2016 Effects of heavy alkali elements in Cu(In,Ga)Se₂ solar cells with efficiencies up to 22.6% *Phys. Status Solidi (RRL)* **10** 583–6
[4] Carron R, Nishiwaki S, Feurer T, Hertwig R, Avancini E, Löckinger J, Yang S-C, Buecheler S and Tiwari A N 2019 Advanced alkali treatments for high-efficiency Cu (In, Ga) Se₂ solar cells on flexible substrates *Adv. Energy Mater.* **9** 1900408
[5] Siebentritt S *et al* 2020 Heavy alkali treatment of Cu(In,Ga)Se₂ solar cells: surface versus bulk effects *Adv. Energy Mater.* **10** 1903752
[6] Wei S-H, Zhang S and Zunger A 1999 Effects of Na on the electrical and structural properties of CuInSe₂ *J. Appl. Phys.* **85** 7214–8
[7] Pianezzi F, Reinhard P, Chirilă A, Bissig B, Nishiwaki S, Buecheler S and Tiwari A N 2014 Unveiling the effects of post-deposition treatment with different alkaline elements on the electronic properties of CIGS thin film solar cells *Phys. Chem. Chem. Phys.* **16** 8843–51
[8] Rockett A 2005 The effect of Na in polycrystalline and epitaxial single-crystal CuIn₁₋ₓGaₓSe₂ *Thin Solid Films* **480** 2–7
[9] Boumenou C K, Phirke H, Rommelfangen J, Audinot J-N, Nishiwaki S, Wirtz T, Carron R and Redinger A 2023 Nanoscale surface analysis reveals origins of enhanced interface passivation in RbF post deposition treated CIGSe solar cells *Adv. Funct. Mater.* **33** 2300590
[10] Elizabeth A *et al* 2022 Surface passivation and detrimental heat-induced diffusion effects in RbF-treated Cu (In, Ga) Se₂ solar cell absorbers *ACS Appl. Mater. Interfaces* **14** 34101–12

[11] Kodalle T, Heinemann M D, Greiner D, Yetkin H A, Klupsch M, Li C, van Aken P A, Lauermann I, Schlatmann R and Kaufmann C A 2018 Elucidating the mechanism of an RbF post deposition treatment in CIGS thin film solar cells *Sol. RRL* **2** 1800156

[12] Wolter M H *et al* 2021 How band tail recombination influences the open-circuit voltage of solar cells *Prog. Photovolt., Res. Appl.* **30** 702–12

[13] Urbach F 1953 The long-wavelength edge of photographic sensitivity and of the electronic absorption of solids *Phys. Rev.* **92** 1324

[14] Pankove J I 1975 *Optical Processes in Semiconductors* (Courier Corporation)

[15] Cody G, Tiedje T, Abeles B, Brooks B and Goldstein Y 1981 Disorder and the optical-absorption edge of hydrogenated amorphous silicon *Phys. Rev. Lett.* **47** 1480

[16] Johnson S and Tiedje T 1995 Temperature dependence of the Urbach edge in GaAs *J. Appl. Phys.* **78** 5609–13

[17] Ramírez O, Nishinaga J, Dingwell F, Wang T, Prot A, Wolter M H, Ranjan V and Siebentritt S 2023 On the origin of tail states and open circuit voltage losses in Cu (In, Ga) Se$_2$ *Sol. RRL* **7** 2300054

[18] Xi J *et al* 2019 Chemical sintering reduced grain boundary defects for stable planar perovskite solar cells *Nano Energy* **56** 741–50

[19] Werner J H, Mattheis J and Rau U 2005 Efficiency limitations of polycrystalline thin film solar cells: case of Cu (In, Ga) Se$_2$ *Thin Solid Films* **480** 399–409

[20] Mattheis U R J, Rau U and Werner J H 2007 Light absorption and emission on semiconductors with band gap fluctuations—a study on Cu(In,Ga)Se$_2$ thin films *J. Appl. Phys.* **101** 113519

[21] Dirnstorfer I, Wagner M, Hofmann D M, Lampert M, Karg F and Meyer B K 1998 Characterization of CuIn (Ga) Se$_2$ thin films *Phys. Status Solidi* a **168** 163–75

[22] Siebentritt S, Rau U, Gharabeiki S, Weiss T P, Prot A, Wang T, Adeleye D, Drahem M and Singh A 2022 Photoluminescence assessment of materials for solar cell absorbers *Faraday Discuss.* **239** 112–29

[23] Rau U, Blank B, Müller T C and Kirchartz T 2017 Efficiency potential of photovoltaic materials and devices unveiled by detailed-balance analysis *Phys. Rev. Appl.* **7** 044016

[24] Gharabeiki S, Melchiorre M and Siebentritt S 2023 Influence of NaF and KF post-deposition treatment on the sub-band gap absorption of Cu (In, Ga) Se$_2$ absorber layers *2023 IEEE 50th Photovoltaic Specialists Conf. (PVSC)* (IEEE) pp 1–3

[25] Jiang C-S, To B, Glynn S, Mahabaduge H, Barnes T and Al-Jassim M M 2016 Recent progress in nanoelectrical characterizations of CdTe and Cu (In, Ga) Se$_2$ *2016 IEEE 43rd Photovoltaic Specialists Conf. (PVSC)* (IEEE) pp 3675–80

[26] Nicoara N, Manalized R, Jackson P, Hariskos D, Witte W, Sozzi G, Menozzi R and Sadewasser S 2019 Direct evidence for grain boundary passivation in Cu (In, Ga) Se$_2$ solar cells through alkali-fluoride post-deposition treatments *Nat. Commun.* **10** 3980

[27] Rau U, Taretto K and Siebentritt S 2009 Grain boundaries in Cu (In, Ga)(Se, S)$_2$ thin-film solar cells *Appl. Phys.* A **96** 221–34

[28] Babbe F *et al* 2023 Vacuum-healing of grain boundaries in sodium-doped CuInSe$_2$ solar cell absorbers *Adv. Energy Mater.* **13** 2204183

[29] Baier R, Lehmann J, Lehmann S, Rissom T, Alexander Kaufmann C, Schwarzmann A, Rosenwaks Y, Lux-Steiner M C and Sadewasser S 2012 Electronic properties of grain boundaries in Cu (In, Ga) Se$_2$ thin films with various Ga-contents *Sol. Energy Mater. Sol. Cells* **103** 86–92

[30] Baier R, Leendertz C, Abou-Ras D, Lux-Steiner M C and Sadewasser S 2014 Properties of electronic potential barriers at grain boundaries in Cu (In, Ga) Se$_2$ thin films *Sol. Energy Mater. Sol. Cells* **130** 124–31

[31] Kim K *et al* 2019 A simple and robust route toward flexible CIGS photovoltaic devices on polymer substrates: atomic level microstructural analysis and local opto-electronic investigation *Sol. Energy Mater. Sol. Cells* **195** 280–90

[32] Hanna G, Glatzel T, Sadewasser S, Ott N, Strunk H P, Rau U and Werner J H 2006 Texture and electronic activity of grain boundaries in Cu (In, Ga) Se$_2$ thin films *Appl. Phys.* A **82** 1–7

[33] Nicoara N, Lepetit T, Arzel L, Harel S, Barreau N and Sadewasser S 2017 Effect of the KF post-deposition treatment on grain boundary properties in Cu (In, Ga) Se$_2$ thin films *Sci. Rep.* **7** 41361

[34] Lanzoni E M, Gallet T, Spindler C, Ramírez O, Boumenou C K, Siebentritt S and Redinger A 2021 The impact of Kelvin probe force microscopy operation modes and environment on grain boundary band bending in perovskite and Cu(In,Ga)Se$_2$ solar cells *Nano Energy* **88** 106270

[35] Caballero R, Kaufmann C, Efimova V, Rissom T, Hoffmann V and Schock H 2013 Investigation of Cu (In, Ga) Se$_2$ thin-film formation during the multi-stage co-evaporation process *Prog. Photovolt., Res. Appl.* **21** 30–46

[36] Siebentritt S *et al* 2021 How photoluminescence can predict the efficiency of solar cells *J. Phys. Mater.* **4** 042010

[37] De Wolf S, Holovsky J, Moon S-J, Löper P, Niesen B, Ledinsky M, Haug F-J, Yum J-H and Ballif C 2014 Organometallic halide perovskites: sharp optical absorption edge and its relation to photovoltaic performance *J. Phys. Chem. Lett.* **5** 1035–9

[38] Wolter M H 2019 Optical investigation of voltage losses in high-efficiency Cu (In, Ga) Se$_2$ thin-film solar cells *PhD Thesis*

[39] Sood M, Urbaniak A, Kameni Boumenou C, Weiss T P, Elanzeery H, Babbe F, Werner F, Melchiorre M and Siebentritt S 2022 Near surface defects: cause of deficit between internal and external open-circuit voltage in solar cells *Prog. Photovolt., Res. Appl.* **30** 263–75

[40] Wolter M H, Bissig B, Avancini E, Carron R, Buecheler S, Jackson P and Siebentritt S 2018 Influence of sodium and rubidium postdeposition treatment on the quasi-fermi level splitting of Cu (In, Ga) Se$_2$ thin films *IEEE J. Photovolt.* **8** 1320–5

[41] Sharma D, Nicoara N, Jackson P, Witte W, Hariskos D and Sadewasser S 2024 Charge-carrier-concentration inhomogeneities in alkali-treated Cu (In, Ga) Se$_2$ revealed by conductive atomic force microscopy tomography *Nat. Energy* **9** 163–71

[42] Krause M *et al* 2020 Microscopic origins of performance losses in highly efficient Cu (In, Ga) Se$_2$ thin-film solar cells *Nat. Commun.* **11** 4189

[43] Maticiuc N, Kodalle T, Lauche J, Wenisch R, Bertram T, Kaufmann C A and Lauermann I 2018 In vacuo XPS investigation of Cu (In, Ga) Se$_2$ surface after RbF post-deposition treatment *Thin Solid Films* **665** 143–7

[44] Taguchi N, Tanaka S and Ishizuka S 2018 Direct insights into RbInSe$_2$ formation at Cu (In, Ga) Se$_2$ thin film surface with RbF postdeposition treatment *Appl. Phys. Lett.* **113** 113903

[45] Cojocaru-Mirédin O, Raghuwanshi M, Wuerz R and Sadewasser S 2021 Grain boundaries in Cu (In, Ga) Se$_2$: a review of composition–electronic property relationships by atom probe tomography and correlative microscopy *Adv. Funct. Mater.* **31** 2103119

[46] Yan Y, Jiang C-S, Noufi R, Wei S-H, Moutinho H and Al-Jassim M 2007 Electrically benign behavior of grain boundaries in polycrystalline CuInSe$_2$ films *Phys. Rev. Lett.* **99** 235504

[47] Beaudoin M, DeVries A, Johnson S R, Laman H and Tiedje T 1997 Optical absorption edge of semi-insulating GaAs and InP at high temperatures *Appl. Phys. Lett.* **70** 3540–2

[48] Ledinsky M, Schönfeldová T, Holovský J, Aydin E, Hájková Z, Landová L, Neyková N, Fejfar A and De Wolf S 2019 Temperature dependence of the urbach energy in lead iodide perovskites *J. Phys. Chem. Lett.* **10** 1368–73

[49] Wasim S *et al* 2001 Effect of structural disorder on the Urbach energy in Cu ternaries *Phys. Rev.* B **64** 195101

[50] Shioda T, Chichibu S, Irie T, Nakanishi H and Kariya T 1996 Influence of nonstoichiometry on the Urbach's tails of absorption spectra for CuInSe$_2$ single crystals *J. Appl. Phys.* **80** 1106–11

[51] Bauknecht A, Siebentritt S, Albert J and Lux-Steiner M C 2001 Radiative recombination via intrinsic defects in Cu$_x$Ga$_y$Se$_2$ *J. Appl. Phys.* **89** 4391–400

[52] Siebentritt S, Gütay L, Regesch D, Aida Y and Deprédurand V 2013 Why do we make Cu(In,Ga)Se$_2$ solar cells non-stoichiometric? *Sol. Energy Mater. Sol. Cells* **119** 18–25

[53] Spindler C, Babbe F, Wolter M H, Ehré F, Santhosh K, Hilgert P, Werner F and Siebentritt S 2019 Electronic defects in Cu (In, Ga) Se$_2$: towards a comprehensive model *Phys. Rev. Mater.* **3** 090302

[54] Zhang S, Wei S-H, Zunger A and Katayama-Yoshida H 1998 Defect physics of the CuInSe$_2$ chalcopyrite semiconductor *Phys. Rev.* B **57** 9642

[55] Siebentritt S, Papathanasiou N and Lux-Steiner M C 2006 Potential fluctuations in compensated chalcopyrites *Physica* B **376–377** 831–3

[56] Larsen J K, Burger K, Gütay L and Siebentritt S 2011 Temperature dependence of potential fluctuations in chalcopyrites *2011 37th IEEE Photovoltaic Specialists Conf.* (IEEE) pp 000396–000401

[57] Shklovskii B I and Efros A L 2013 *Electronic Properties of Doped Semiconductors* (Springer Science & Business Media)

[58] Rey G, Larramona G, Bourdais S, Choné C, Delatouche B, Jacob A, Dennler G and Siebentritt S 2018 On the origin of band-tails in kesterite *Sol. Energy Mater. Sol. Cells* **179** 142–51

[59] Gokmen T, Gunawan O, Todorov T K and Mitzi D B 2013 Band tailing and efficiency limitation in kesterite solar cells *Appl. Phys. Lett.* **103** 103506

[60] Schroeder D J and Rockett A A 1997 Electronic effects of sodium in epitaxial CuIn$_{1-x}$Ga$_x$Se$_2$ *J. Appl. Phys.* **82** 4982–5

[61] Yuan Z-K, Chen S, Xie Y, Park J-S, Xiang H, Gong X-G and Wei S-H 2016 Na-diffusion enhanced p-type conductivity in Cu (In, Ga) Se$_2$: a new mechanism for efficient doping in semiconductors *Adv. Energy Mater.* **6** 1601191

[62] Colombara D, Stanbery B J and Sozzi G 2023 Revani diffusion model in Cu (In, Ga) Se$_2$ *J. Mater. Chem.* A **11** 26426–34

[63] Schuler S, Siebentritt S, Nishiwaki S, Rega N, Beckmann J, Brehme S and Lux-Steiner M C 2004 Self-compensation of intrinsic defects in the ternary semiconductor CuGaSe$_2$ *Phys. Rev.* B **69** 045210

[64] Abou-Ras D, Schäfer N, Hages C J, Levcenko S, Márquez J and Unold T 2018 Inhomogeneities in Cu (In, Ga) Se$_2$ thin films for solar cells: band-gap versus potential fluctuations *Sol. RRL* **2** 1700199

[65] Wang T, Ehre F, Weiss T P, Veith-Wolf B, Titova V, Valle N, Melchiorre M, Ramírez O, Schmidt J and Siebentritt S 2022 Diode factor in solar cells with metastable defects and Back contact recombination *Adv. Energy Mater.* **12** 2202076

[66] Wang T *et al* 2024 Shifting the paradigm: a functional hole-selective transport layer for chalcopyrite solar cells *Sol. RRL* **8** 2400212

[67] Wurfel P 1982 The chemical potential of radiation *J. Phys. C: Solid State Phys.* **15** 3967

[68] Gharabeiki S, Schaff T, Lodola F, wang T, Melchiorre M and Siebentritt S Exact determination of quasi-Fermi level splitting in the Cu(In,Ga)Se$_2$ absorbers *Under preparation*

[69] Daub E and Wurfel P 1995 Ultralow values of the absorption coefficient of Si obtained from luminescence *Phys. Rev. Lett.* **74** 1020–3